Annals of Biomedical Engineering, Vol. 33, No. 3, March 2005 (© 2005) pp. 284–300
DOI: 10.1007/s10439-005-1731-0

Physics-Driven CFD Modeling of Complex Anatomical Cardiovascular Flows—A TCPC Case Study

KEREM PEKKAN,[1] DIANE DE ZÉLICOURT,[1] LIANG GE,[2] FOTIS SOTIROPOULOS,[2] DAVID FRAKES,[1] MARK A. FOGEL,[3] and AJIT P. YOGANATHAN[1]

[1]Wallace H. Coulter Department of Biomedical Engineering, Atlanta, GA; [2]School of Civil and Environmental Engineering, Georgia Institute of Technology, GA; and [3]Division of Cardiology, The Children's Hospital of Philadelphia, PA

(Received 3 May 2004; accepted 28 September 2004)

Abstract—Recent developments in medical image acquisition combined with the latest advancements in numerical methods for solving the Navier-Stokes equations have created unprecedented opportunities for developing simple and reliable computational fluid dynamics (CFD) tools for meeting patient-specific surgical planning objectives. However, for CFD to reach its full potential and gain the trust and confidence of medical practitioners, physics-driven numerical modeling is required. This study reports on the experience gained from an ongoing integrated CFD modeling effort aimed at developing an advanced numerical simulation tool capable of accurately predicting flow characteristics in an anatomically correct total cavopulmonary connection (TCPC). An anatomical intra-atrial TCPC model is reconstructed from a stack of magnetic resonance (MR) images acquired *in vivo*. An exact replica of the computational geometry was built using transparent rapid prototyping. Following the same approach as in earlier studies on idealized models, flow structures, pressure drops, and energy losses were assessed both numerically and experimentally, then compared. Numerical studies were performed with both a first-order accurate commercial software and a recently developed, second-order accurate, in-house flow solver. The commercial CFD model could, with reasonable accuracy, capture global flow quantities of interest such as control volume power losses and pressure drops and time-averaged flow patterns. However, for steady inflow conditions, both flow visualization experiments and particle image velocimetry (PIV) measurements revealed unsteady, complex, and highly 3D flow structures, which could not be captured by this numerical model with the available computational resources and additional modeling efforts that are described. Preliminary time-accurate computations with the in-house flow solver were shown to capture for the first time these complex flow features and yielded solutions in good agreement with the experimental observations. Flow fields obtained were similar for the studied total cardiac output range (1–3 l/min); however hydrodynamic power loss increased dramatically with increasing cardiac output, suggesting significant energy demand at exercise conditions. The simulation of cardiovascular flows poses a formidable challenge to even the most advanced CFD tools currently available. A successful prediction requires a two-pronged, physics-based approach, which integrates high-resolution CFD tools and high-resolution laboratory measurements.

Address correspondence to Ajit P. Yoganathan, PhD, Wallace H. Coulter School of Biomedical Engineering, Georgia Institute of Technology & Emory University, Room 2119 U. A. Whitaker Building, 313 Ferst Dr. Atlanta, GA 30332-0535. Electronic mail: ajit.yoganathan@bme.gatech.edu

Keywords—Fontan operation, Digital Particle Image Velocimetry (DPIV), Flow instability, Computational Fluid Dynamics (CFD), Exact replicate models, Patient specific, Surgical planning, Total Cavopulmonary Connection (TCPC).

INTRODUCTION

Developments in medical image acquisition and processing have enabled hemodynamic analysis of patient-specific anatomic geometries. Computational fluid dynamics (CFD) has appeared to be a useful tool by producing practical flow solutions that realize fast explorative studies. Particular research areas include blood flow through the carotid artery,[4] detailed aortic arch models,[55] aneurysms,[34] embryonic heart development,[9] left ventricle models,[54] cerebral flows and cavities,[49] surgical anastomosis and graft designs,[40] coronary arteries,[36] flow through large airways and lungs,[48] and coupled lumped-flow and anatomy studies.[15] Additional studies of interest have been presented in specific workshops.[33,65] As emphasized in recent editorial remarks,[44,64] however, for CFD to realize its full potential as a powerful clinical tool for patient-specific modeling, there is a pressing need for rigorous model validation with detailed laboratory data. Using numerical simulation tools void of comprehensive experimental validation to make important surgical or clinical decisions could be a dangerous practice. Simply put, such tools could yield solutions that are hemodynamically irrelevant and fail to capture even the basic features of the actual flow.

The broader fluids engineering community has always been skeptical about the credibility of numerical solutions that have either been obtained with low-resolution techniques and/or lack ground-truth experimental validation. On many occasions,[58,62,5] the limitations of CFD tools have been documented,[20,41] and the need for high-resolution numerical schemes, comprehensive experimental validation, and careful applications have been reinforced.[19] Compared to most areas of engineering where CFD has made a major impact (aerodynamics, ship hydrodynamics,

turbomachinery, etc.), biomedical engineering involves flows with a host of unique modeling challenges and difficulties. Such flows take place in complex, multiconnected domains with compliant walls and flexible immersed boundaries and are dominated, among other factors, by pulsatile effects, three-dimensional separation and vortex formation, regions of flow reversal, periodic transition to turbulence and laminarization, and non-Newtonian effects. In spite of these enormous complexities, which pose a formidable challenge to even the most advanced CFD tools available today, the notion that CFD is a mature technology that can be applied indiscriminately to model any flow physics is becoming *de facto* in the biomedical field. In reality, CFD for complex cardiovascular flows is an intricate and continuously evolving science that necessitates a synergy between modeling efforts and *in vitro* experimentation to guide model development and validation.

Blood flow in the total cavopulmonary connection (TCPC) morphologies, which is the primary focus of this paper, serves as an excellent example for illustrating the aforementioned complexities and modeling challenges. The TCPC is the current procedure of choice for surgical repair of single ventricle heart disease.[8] A good historical background on Fontan surgery is provided by Friesen and Forbess,[22] which involves the anastomosis of inferior and superior venae cavae directly to the pulmonary arteries, bypassing the right side of the heart in order to avoid mixing oxygenated and deoxygenated blood. Even though postrepair survival rates have been steadily improving, patients are still susceptible to numerous complications[6,27] (limited exercise capacity, progressive cyanosis from pulmonary arteriovenous malformations, systemic to hepatic venous malformations or atrial level shunting, thromboembolism, atrial and ventricular arrhythmias, and protein losing enteropathy). Earlier studies have demonstrated that the geometric configuration of the TCPC is a primary factor in determining the efficiency of the connection and in turn, postoperative outcomes.[11] The TCPC anatomy, complex and highly variable among patients, is a good test case to illustrate CFD modeling advances that can be generalized to other complex cardiovascular flows.

Idealized models of the TCPC[63,53] simplified the central connection region, which is located upstream of the pulmonary artery (PA) branches and downstream of the innominate and hepatic veins, as a "+" shape formed by the intersection of four smooth vessels of constant diameters. Two of these vessels serve as inlets and two as outlets. The most sophisticated configuration is currently the combined model by Liu *et al.*,[42] which incorporated all of the main anatomic features, such as caval offset, caval diameters, vessel flaring and/or curvature, with the exception of PA branching.[57] Fluid-structure interaction and tissue/graft material mismatch in TCPC configurations are also studied.[43] Though these studies provided some insight into the relative impact of different geometric parameters of the connection, we believe that more accurate patient-specific models of the connection geometry are needed for a complete understanding of the TCPC and for future surgical planning applications.

Because the patients who undergo the TCPC procedure are usually young, small anatomical regions of interest and abbreviated scan times are involved, requiring specialized reconstruction procedures[16] and limit the number of anatomical TCPC flow studies in literature. Kim *et al.*[39] investigated atriopulmonary and cavopulmonary connections based on magnetic resonance imaging (MRI) and computer tomography (CT) scans using realistic glass replicas of the anatomy where laser Doppler anemometry and pressure measurements identified complex swirling flows and large pressure drops associated with the superior vena cava (SVC) to main pulmonary artery (MPA) transition. *In vivo* magnetic resonance phase contrast imaging (PC-MRI) has been a valuable tool[13] for TCPC research, as it provides semiquantitative and qualitative flow field information.[24] PC-MRI studies in *in vivo* TCPC geometries have captured central flow stagnation regions resulting from the collision of SVC and inferior vena cava (IVC) streams, and have confirmed the relationship between caval offset and efficiency.[56] Studies on realistic TCPC anatomies,[25,46] using computational fluid dynamics as the main tool, have outlined the concept of surgical planning. Recently, Migliavacca *et al.*[45] compared four alternative inferior vena cava (IVC) geometries for a given Glenn stage anatomy and reported the basic technical limitations in their complex pulsatile simulations. While such studies produced comparative conclusions and qualitative flow visualization, experimentally validated CFD models are critical and should ultimately be used in assessing hemodynamic performance. Even at the relatively simple step of CFD model verification, significant differences in results were found depending on the grid generation schemes used.[42] These differences are reported for anatomically realistic, idealized models with combined features in steady-state flow conditions. Transient flow and complex morphologies present additional verification issues that have not yet been addressed in the literature. Based on our MRI research database, TCPC anatomies can be roughly grouped into five main templates (extra-cardiac conduit, intra-atrial tunnel, bilateral SVC, interrupted IVC, and IVC to MPA). At least one comprehensive *in vitro* experimental campaign per template is needed for a good understanding of the flow phenomena and for CFD tool validation before using CFD for surgical design. Towards that end, this paper describes a combined experimental and numerical *in vitro* analysis methodology for a selected intra-atrial TCPC anatomy containing an unusually large "pouch" shape connection. The morphology and corresponding flow complexity introduced new challenges both for the numerical and experimental efforts. The results of this work suggest a cautious approach in the use of available CFD tools and indicate that

high-resolution CFD techniques specifically tailored to tackle the complexities of cardiovascular flows are necessary.

The paper is organized as follows. In Anatomy section we describe the TCPC anatomy and outline the reconstruction method. In *In Vitro* Experiments section we describe the experimental techniques and data processing procedures used for the *in vitro* experiments. In Computational Model section we describe briefly the two CFD models employed in this work and discuss various computational details. In Results section we present and discuss the experimental and computational results and in Discussion and Conclusions sections we summarize our findings and the conclusions of our work.

ANATOMY

Reconstruction

A 9-year-old child with an intra-atrial TCPC connection was imaged via an MRI system (Sonata, Siemens, Malvern, PA). Informed consent was obtained and all related studies were approved by the internal review board at the Children's Hospital of Philadelphia. Twenty T1-weighted axial images were acquired, spanning the entire connection region. The MRI scanning parameters used in conjunction with this work are as follows: static true-FISP pulse sequence with slices = 40–50 without a gap encoding the phase A→P, slice thickness = 4–5 mm, FOV = 200–400 mm, TR = 140–200 ms, line TE = 1.3 ms, averages = 3, flip angle = 65–90 degrees, matrix 92 × 256 to 128 × 256, echo spacing = 2.9 ms, bandwidth = 1120/Hz/px, contrast was not used. In order to counteract the out-of-plane sampling limitations inherent to MRI, a technique called adaptive control grid interpolation was used to enhance the image stack.[16] This process produces a data volume composed exclusively of isotropic voxels. Following enhancement, the vessels of interest were segmented from the data volume using an in-house code. Here a special case of region growing called shape element segmentation was employed to isolate the vascular area of interest in multiple image planes with high consistency.[18] The three-dimensional representation of the TCPC was ultimately generated in Mimics (Materialise Inc., Ann Arbor, MI), as presented in Fig. 1.

The characteristic dimensions of the intra-atrial TCPC obtained were considerably smaller than those from previous studies in TCPC literature. Liu *et al.*[42] and Ryu *et al.*[53] had already studied idealized models mimicking anatomical diameters. Both proposed a SVC and IVC of 8 mm and 15 mm, respectively, and PA diameters of 13.335 mm. However, in our reconstructed geometry, the hydraulic diameters 2 cm away from the connection area were only 5.1 mm, 4.2 mm, 4.2 mm, and 12.4 mm, for the RPA, LPA, SVC, and IVC, respectively. The connection site had a pouch shape with a hydraulic diameter of 18 mm, and all vessels were enlarged towards the anastomosis site. Typically the

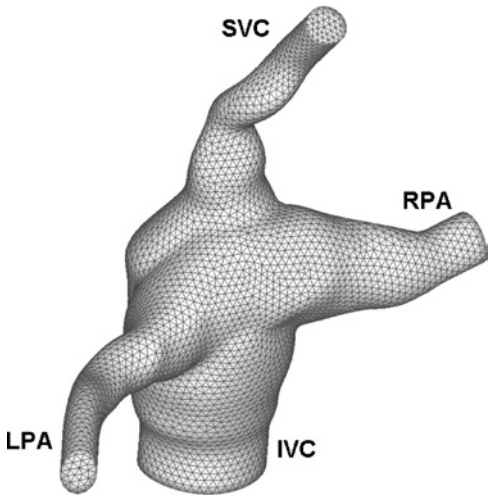

FIGURE 1. Coarse unstructured grid of the intra-atrial Fontan connection, 64,836 tetrahedral elements.

LPA diameter ranged from 10.8 mm at the anastomosis site to 4.2 mm at 2 cm downstream of the connection. In the same manner, the SVC and RPA connected to the pouch with a hydraulic diameter of 8.5 and 8.2 mm, respectively, but quickly tapered down to the dimensions mentioned previously. As in the previous study by Ryu *et al.*,[53] all four vessels were not coplanar. While both the IVC and RPA occupied the coronal plane, the SVC and LPA bent in the posterior direction, forming an angle of 48° and 37° with the IVC-RPA plane, respectively. This reconstructed geometry was used for both CFD and experimental purposes. The complexity of the geometry, as well as its small dimensions, conditioned the complex flow behavior that took place in this specific TCPC.

CAD and Stereolithography

For a complementary *in vitro* experimental and CFD study involving complex MRI-acquired morphologies, an accurate prototype production methodology is the first requirement. The *in vitro* prototypes must be optically clear for quantitative flow measurement techniques such as laser Doppler velocimetry (LDV) and PIV. With glass blowing techniques, patient-specific experimental models can only be approximately reproduced, depending on operator skill. Rapid prototyping (RP) technology[59,35] eliminates operator dependence, and exact replication of the anatomy from computer-aided design (CAD) data becomes possible. Optically clear models may then be obtained with Sylgard or silicone RTV based materials, but only through tedious casting and accurately controlled curing processes.[2,66] Our approach to this problem was to use the recently available "transparent" RP resins as an *in vitro* anatomic model material, thus making possible a direct one-step "printout" of the morphology from the anatomic CAD file. With this single-step novel approach, exact replicates of the CFD models

are put *rapidly* to benchtop *in vitro* testing. This technique is particularly well-suited for small regions of interest, such as the TCPC, and can enable patient-based analyses on a large scale.

A major advantage of RP techniques is that CAD data can be directly provided as input for further CAD and modeling operations. Originally, as they were imaged, the vessels of our anatomical model were no more than 2 cm long. Clean cross-sections were obtained by cutting each of the vessels orthogonally to their axis, and were then used as a basis to extrude pulmonary arteries and vena cavae over a distance sufficient for both numerical and experimental purposes. While the extended lumen model could be transferred to grid generation, the actual experimental model was generated by Boolean subtraction of the extended TCPC lumen from a solid box. The main constraints for box design were to avoid image distortion and laser light scattering when performing PIV. All angles in the box were designed to be away from the region of interest; the outer surfaces that would be facing the camera and the laser were made flat and orthogonal to the desired acquisition and laser beam axis.

Stereolithographic techniques generate construction supports under all overhanging surfaces. Thus, had the model been constructed as a single block, supports would have been built throughout the entire blood volume. Though easy to remove these supports significantly alter the inside surface and would have impaired the optical quality as well as the geometrical accuracy of our model. Therefore, the box was split into two parts along the axis of the vessels. These were then glued back together using epoxy glue, which was less expensive than the available UV-curing techniques and had no significant impact on data acquisition.

The model was manufactured using an SLA®250 (3D Systems, Valencia, CA) system, with Renshape 5510 transparent resin (Vantico AG, Basle, Switzerland) and a build accuracy of 0.004 in. (0.1 mm). No chemical curing was performed. Stereolithographic techniques cure the resin by layers, thus generating ridges of the same thickness as the set accuracy that can be removed with thorough polishing. Since this study focused on CFD validation, the priority was set on geometric accuracy between the numerical and experimental models. Given the small dimensions of the intra-atrial TCPC considered here, the model was left "as is" so as not to alter the anatomy. As rapid prototyping resins came out of the machines, their surfaces were slightly blurry. This was overcome for the inner surfaces by matching the refractive index of the working fluid and by polishing the outer surfaces, first with wet sandpaper of decreasing grain size (400 and 600) and then with coarse and fine polishing compounds (No. 7 "rubbing compound" and No. 7 "Clearcoat polishing compound," respectively). As a final step, before *in vitro* experiments, transparency was improved by spraying a transparent acrylic paint (Rust Oleum "Gloss Clear 1901") over the closed box.

IN VITRO EXPERIMENTS

Pressure Measurements

All experiments were run under steady inflow conditions maintained by a constant pressure head. Four rotameters (Dakota Instruments, Monsey, NY) were used to assess the total flow rate, the IVC flow, and each of the pulmonary flows. Total cardiac output ranged from 1 to 3 l/min. The SVC/IVC flow ratio was fixed at 40/60 to reflect the physiological flow splits seen in children[14] while the RPA/LPA ratio was varied from 30/70 to 70/30 by 10% increments in order to simulate varied pulmonary resistances. Pulmonary flow readings were taken on the PA that had the highest share of the flow in order to ensure optimal reading accuracy. A fully developed inflow profile was achieved by connecting extension pipes of 50 vessel diameters in length to both the IVC and SVC. A solution of water-glycerin reproduced the kinematic viscosity of blood ($\nu = 3.5 \pm 0.1$ cSt). Viscosity was checked using a Cannon-Fenske routine viscometer (Fisher Scientific, Pittsburg, PA).

Static pressure was assessed at the wall of each vessel 10 cm away from the center of the connection. Three multiple range differential pressure transducers (Model DP15, Validyne Engineering, Northridge, CA), calibrated for a range of 0–40 mm Hg, were used to measure the pressures in each one of the LPA, RPA, and SVC with respect to the IVC pressure. The transducer signal was amplified (Model CD19, Validyne Engineering, Northridge, CA) and then interfaced to an A/D board (DAQCard 1200, National Instruments Corp., Austin, TX). Pressure data were collected on a PC using an in-house software package. The data were acquired at a rate of 500 Hz over 10 s and averaged to produce a single value for static pressure to increase accuracy. At any given total flow rate and flow split, the transducers were rotated and measurements were performed in sequence by each one of the three differential pressure transducers (SVC/IVC, LPA/IVC, RPA/IVC), so as to remove any transducer bias. Each experiment was repeated eight times. This provided 24 static differential pressure data sets per location, flow split, and flow rate. Each data set was used to compute the 24 corresponding control volume power losses, which were then averaged as one single value with the corresponding standard deviation.

Data Processing

For both experimental and CFD studies, only the power losses occurring in the same size connection region were considered. However, for experimental convenience, pressures were acquired further downstream. Assuming that all pressure drops occurring in the extension pipes were due to friction, the experimental pressure data were corrected using the following formula:

$$P_{\text{corrected}} = P_{\text{measured}} - \Delta P_f \tag{1}$$

where ΔP_f is the friction pressure loss and is calculated as follows:

$$\Delta P_f = (\lambda/d_h)(\rho V^2/2)L \quad (2)$$

For laminar flow ($Re < 2300$), λ is $64/Re$, ρ is the density of the working fluid, V the velocity (considered as being the average velocity through the vessel and obtained by dividing the flow rate by the cross-sectional area), and L is the length of the extension pipe between the end of the anatomy as in the MRI reconstruction and the pressure acquisition point. The branch Reynolds numbers, Re, are based on average flow velocity, V, and the hydraulic lumen diameter, d_h.

Experimental pressure drops were also corrected for pressure head effects. Prior to experimentation, differential pressures were acquired with still fluid in the loop (P_0). To improve experimental reproducibility, this P_0 value was retrieved from all subsequent pressure measurements so as to remove any pressure head bias that could have been introduced by a small change in the model elevation. Finally the static pressures used in the power loss calculations were obtained with the following formula:

$$P_{\text{static}} = P_{\text{measured}} - \Delta P_f - P_0 \quad (3)$$

Using Bernoulli's theorem, the total pressures were computed as follows:

$$P_{\text{total}} = P_{\text{static}} + P_{\text{kinematic}} = P_{\text{static}} + 1/2\,\rho V^2 \quad (4)$$

Energy losses were then computed by an integrated control volume energy balance:

$$\dot{E}_{\text{loss}} = \sum_{\text{inlet}} P_{i\,\text{total}}\, Q_i - \sum_{\text{outlet}} P_{i\,\text{total}} Q_i \quad (5)$$

where $P_{i\,\text{total}}$ and Q_i are the total pressure and the flow rate respectively at an inlet (i = IVC, SVC) or an outlet (i = LPA, RPA).

Flow Visualization

Control volume pressure drops and power losses enable quantitative macroscopic comparison but provide no further insight into flow structures. For that purpose, flow visualization experiments were performed in the anatomical intra-atrial model. The flow conditions and experimental setup were identical to those of the pressure measurements. Catheters were inserted into the IVC and SVC 5 cm upstream of the model and driven down to the opening of the connection. A mixture of liquid soap and dry pigments was injected through the catheters to generate streaklines. The model was illuminated from one side with a halogen lamp while the images were acquired from the other side with a CCD camera at 500 frame/s. A blank white paper sheet located between the halogen lamp and the model acted as a diffuser and prevented the flow visualization images from being overexposed.

Particle Image Velocimetry

DPIV was also performed on the anatomical model. We used a TSI system (TSI Inc., Shoreview, MN), which included a data acquisition software package (Insight 3.34), two 17 mJ miniYag lasers ($\lambda = 514$ nm) and one camera. The fluid was seeded with melamine-formaldehyde spheres and dyed throughout the volume with Rhodamine B (MF/RhB, size range: 2.5–5 μm, Microparticles GmbH, Berlin, Germany). As the emission spectra of RhB peak is around 590 nm, a red color filter ($\lambda = 570$ nm) was used to cut off the laser beam reflections on the model surfaces while still allowing the fluorescent particles to shine through. An aqueous solution of glycerin and sodium iodide was used to match both the kinematic viscosity of blood ($\nu = 3.5 \pm 0.1$ cSt) and the refractive index of the resin ($n = 1.51$).

Velocity data were acquired in the coronal plane. Three hundred double frames were acquired at each location at 15 Hz. The selection of 300 pairs was aimed at obtaining a representative mean field. As an accuracy check we processed the batch of data with different number of frames: 10, 50, 100, 150, 200, 250, and 300. The variation between the average obtained with 200 and with 300 frames is less than 5%, and the variation between 250 and 300 is less than 2.5%. It was thus considered that sufficient convergence of the running average was achieved with 300 frames. Moreover when acquiring more than 300 double frames (which could have been possible) storage of data becomes a serious issue; 300 was thus a tradeoff between convergence and data storage space.

Cross-correlation vectors were computed with DaVis 6.2.2 (LaVision Gmbh, Gottingen, Germany). A mask was applied to filter out the region of interest. The vectors were computed using the Fast Fourier Transform without zero padding in multiple passes. The interrogation window is progressively decreased (64×64 pixels down to 16×16 pixels) and a 50% overlap window was specified, satisfying the Nyquist condition. Intermediate flow fields were smoothed out, but no smoothing was applied after the last pass. The 300 instantaneous flow fields were averaged into a single frame.

COMPUTATIONAL MODEL

Computational Fluid Dynamics of the anatomy were studied for the same experimental conditions, namely incompressible, laminar flow with steady inflow conditions and rigid vessel walls. Calculations were carried out with two different flow solvers: the commercial CFD package FIDAP and a recently developed, in-house, high-resolution unsteady flow solver, which will be subsequently referred to as the *in-house code*. The FIDAP computations were aimed at exploring the accuracy with which a state-of-the-art commercial code can predict the general flow patterns

and in particular the energy losses for various flow splits and Reynolds numbers. The simulations with the in-house code were prompted by the finding that even though the steady FIDAP solutions captured the global, time-averaged features of the laboratory flow with reasonable accuracy they did not yield the experimentally documented complex, unsteady flow patterns in the connection region with the available computational resources. Note that in spite of using steady inflow conditions, unsteadiness in the laboratory flow emerged naturally (without any external forcing through the boundary conditions) due to inherent flow instabilities. The in-house code simulations are preliminary, pending numerical sensitivity studies, but capture for the first time the onset of unsteadiness in the connection region and yield a time-averaged flow which is in reasonable agreement with the measurements. Throughout this study, feedback between the experimental and computational studies was crucial and enabled a thorough understanding of the underlying flow phenomena.

The Commercial Flow Solver

The parallelized segregated finite-element solver FIDAP (Fluent Inc., Lebanon, NH) with the SIMPLER-like pressure projection algorithm[28] was used in conjunction with the conjugate gradient (CG) and conjugate gradient squared (CGS) iterative solvers for symmetric and nonsymmetric linear equations with Gauss-Seidel and diagonal preconditioning, respectively. Petrov–Galerkin pressure stabilization was activated for the 4-node linear unstructured tetrahedrons.[32] The streamline upwind scheme,[31] which enables better-than-first-order accuracy in the cross-stream direction, was utilized to discretize the convective terms. The overall accuracy of this scheme, however, is only first-order.

All simulations with FIDAP converged to a steady-state solution starting from a zero initial guess. The residuals leveled off after approximately 800 iterations, as the velocity residuals decreased by three orders of magnitude and the pressure residuals decreased by four orders of magnitude. The iteration process was continued, however, for 3000 iterations to ensure that convergence was indeed achieved and that no long term instabilities develop. Convergence criteria for the CG and CGS systems were 0.01 and 0.001 times the residual convergence criteria with an appropriate number of inner iterations, respectively.

All jobs were run in parallel with 2- or 4-CPU nodes in linux (2.8 GHz) and Sun (450 MHz) machines with 2–4 GBytes memories. Mesh partitioning was done through PMETIS[37] and DOMEC[12] schemes with little difference in CPU time. For the medium grid a typical convergence required 32 CPU hours. For comparison, for the in-house flow solver an equivalent calculation took around a week to get a statistically converged solution on an AMD XP 2800+ machine.

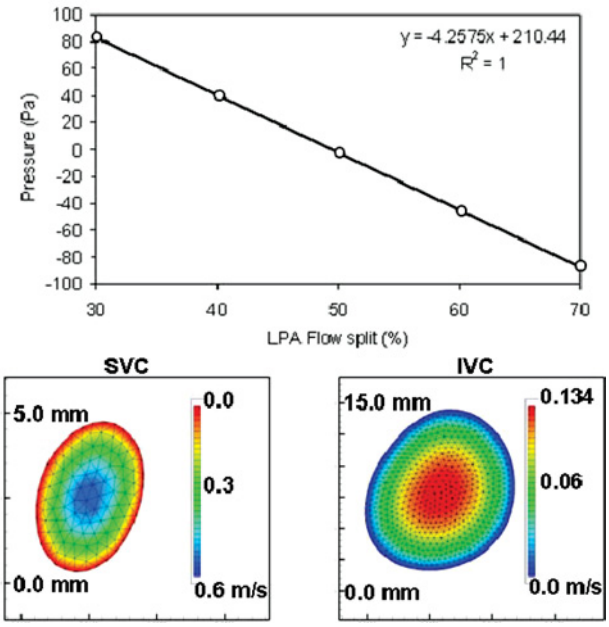

FIGURE 2. Boundary conditions. Bottom-Left and Bottom-Right are inflow velocity profiles (axial-component) at SVC and IVC, resepctively. Top: LPA pressure-flow rate correlation for correct PA flow split specification.

Steady inflow boundary conditions were specified at the IVC and SVC. The total cardiac output was split 60:40 between the IVC and SVC. At both vena cavae the inflow velocity profile was specified as fully developed. To obtain the specific fully developed velocity profile, auxiliary steady CFD solutions were performed over the inlet entrance lengths (since the anatomic vessel cross-sections were not exactly circular, the actual fully developed flow profile was an unknown). Computations with the uniform plug-flow velocity profile did not reproduce the experimental DPIV flow field. Reasonable agreement with experimental results was only achieved when the fully developed flow profiles of the experimental conditions were implemented. Outflow through the PAs was modeled using pressure boundary conditions. To specify the correct split, a set of auxiliary runs, as shown in Fig. 2, were performed to map the pressure and PA split characteristics of the connection.[42]

The In-House Flow Solver

As discussed above, the laboratory experiments showed that even with steady inflow conditions, a very complex, unsteady flow emerges naturally in the region where the IVC and SVC flows collide. The unsteadiness appears to be the result of a stagnation-point instability, which is dominated by high-frequency modes and manifests itself as a seemingly chaotic meandering and flapping of the flow in the connection region. This kind of instability, which is essentially identical to that reported in idealized TCPC connections in previous experimental[38] and computational

studies,[3] was found to occur for all inflow conditions considered in this work. Yet for all simulated cases, the FIDAP code converged to steady state solutions, thus, failing to capture this important feature of the laboratory flow. An attempt to carry out time-resolved, unsteady simulations with FIDAP, which is an option available in the code, was not conclusive. Running FIDAP in unsteady mode required a very small time step and excessive computational resources which were beyond those at our disposal. Consequently the computations could not be continued long enough to establish whether physical unsteady flow patterns emerged and were sustained over a long time interval.

To explore whether the onset of unsteady flow could indeed be predicted numerically, we carried out a simulation using a recently developed, in-house CFD code. The numerical method is that developed by Ge *et al.*[23] for simulating flows in mechanical, prosthetic heart valves. It employs domain decomposition with overset (Chimera) meshes[23,60] to discretize arbitrarily complex, multiconnected domains with domain-structured, body-fitted meshes. The governing equations are discretized on a nonstaggered grid in strong-conservation form using second-order accurate numerics. Namely, three-point, second-order accurate central-differencing plus third-order, fourth-difference, matrix-valued artificial dissipation is used for the convective terms while central differencing is used for the remaining terms in the governing equations. The discrete equations are integrated in time using a dual-time stepping, artificial compressibility technique in conjunction with a block, approximate-factorization iterative algorithm for rapid convergence during each physical time step. At the exit of the LPA/RPA, the velocity components are adjusted by a scaling factor to obtain the same mass flux split ratio as used in the experiments. Transient simulations are continued until a steady-state running average in all the flow variables is established; this roughly corresponds to 5000 time steps.

It is important to point out that, unlike the commercial code, running the in-house code in a steady-state mode failed to yield converged solutions. Based on our past experience with this code, failing to obtain a converged steady-state solution typically means that the physical flow is likely to be inherently unstable and flow unsteadiness is to be anticipated. For that reason we began running the code in an unsteady mode, using the dual-time iterative algorithm to converge the velocity and pressure residuals by approximately two to three orders of magnitude per physical time step. Upon switching to the unsteady mode of the code, we found that a complex, unsteady solution naturally emerged, which exhibited many of the attributes of the laboratory flow.

Grid Generation

For the FIDAP computations, a systematic grid refinement study was carried out using three gradually refined grid sets with 64,000 to 340,000 tetrahedral elements, respectively (see Fig. 1 for a typical view of the FIDAP computational mesh). The results of the grid refinement study are discussed in Results section below.

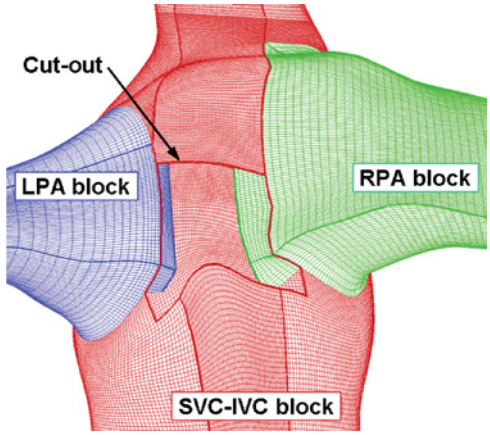

FIGURE 3. Fine structured overset grid, made of three blocks, which is used with the in-house complex flow solver. A cutout is provided on the surface of the SVC-IVC block to show the overlapping LPA and RPA domains.

For the in-house code a Chimera overset mesh was generated consisting of three block-structured grids (LPA arm, RPA arm, and IVC/SVC conduit) with a total of 1.18 million nodes. The meshes in each subdomain were generated using the Gridgen (Pointwise Inc, Fort Worth, TX) commercial grid-generation software. A typical view of the overset mesh is shown in Fig. 3. The entire complex lumen geometry is spanned by 74 individual structured surface domains. For geometry as complex as that studied in this work, generating a good quality (grid stretching ratios $\leq$1.2 and the grid aspect ratios $\leq$300) block structured mesh typically requires 40 times more effort than generating the unstructured mesh used by FIDAP.

Ten-node tetrahedral elements with ultra fine grids ($\sim$800,000 elements) are also employed with FIDAP in an effort to obtain time-dependent simulations with higher spatial resolution and second-order accuracy. However these studies challenged our current computational capabilities to their limit and the calculations could not be completed in a reasonable amount of time.

RESULTS

For the fixed IVC/SVC ratio, results were gathered over the hemodynamic operation range of the anatomic TCPC connection. This range corresponds to the five measurement runs at each cardiac output (RPA to LPA ratios used were 70/30, 60/40, 50/50, 40/60, and 30/70), which are summarized in Table 1. All these operating conditions were studied experimentally using flow visualization and DPIV. Numerical simulations, however, were carried out only for those operating conditions for which the flow remains laminar.

TABLE 1. Case identification numbers for all studied flow conditions, e.g., Case 21 denotes 30/70 flow split at 2 l/min total cardiac output conditions and IVC/SVC split is 60/40 for all these cases.

Cardiac output (l/min)	Flow split RPA/LPA				
	30/70	40/60	50/50	60/40	70/30
1	11	12	13	14	15
2	21	22	23	24	25
3	31	32	33	34	35

Modeling turbulent flows in such a complex configuration is a far more demanding undertaking and will be left as a topic for future research. Steady-state solutions were obtained with FIDAP for all measured operating points in the laminar flow regime (Cases 11, 12, 13, 14, 15, 21, 22, 23, 24, 25, 33, and 34 in Table 1). Due to the higher computational overhead per simulation, the very fine mesh employed and the time-accurate solution procedure, the in-house code was employed to carry out an unsteady simulation for only one operating point (Case 13 in Table 1).

In the subsequent sections, the computed solutions are compared with each other and measurements in the following order. First, we compare predicted, steady-state energy losses obtained with FIDAP with those extracted from time-averaged experimental measurements (see Data Processing section) for all simulated points. Next, we compare the steady flow predictions of FIDAP for the velocity magnitude with the time-averaged results from the in-house code simulations and the DPIV measurements at various planes through the connection for Case 13. Finally, we discuss the complex, unsteady characteristics of the flow as documented in the flow visualization experiments and compare flow visualization images with instantaneous particle traces obtained from the unsteady simulation with the in-house code. Presenting our results in this fashion is intended to underscore an important finding of our work, namely that even though a reasonable description of time-averaged flow quantities can be obtained using commercially available CFD models that employ first-order discretization schemes that are similar to FIDAP, predicting the details of the instantaneous flow is a far more challenging and demanding task that requires considerably more careful and sophisticated modeling.

Model Validation with Time-Averaged Flow Quantities

Control Volume Power Losses

The hydrodynamic power loss variation, Eq. (5), for the anatomical intra-atrial TCPC is plotted in Fig. 4 for 1, 2, and 3 l/min. Both computational (steady-state with FIDAP) and experimental data demonstrated similar trends of energy loss as a function of RPA/LPA split. The experimental variation in Fig. 4 is presented with a 98% confidence limit. The steady laminar numerical solutions with FIDAP fell within this error band for all cardiac outputs. For 3 l/min, CFD power losses calculated with the steady-flow model were only 5% higher than their experimental mean. Power loss value calculated by the in-house code (8.02 mW), at 1 l/min and at equal LPA/RPA split (Case 13), is also found to be within the tight experimental error range of this cardiac output.

Figure 4 also shows the results of the previously discussed grid refinement study with FIDAP. For the 1 l/min case all three meshes with 64836 (coarse), 147721 (medium), and 340315 (fine) tetrahedral elements yielded essentially identical results, which implies that even the coarsest mesh is adequate to establish a grid independent numerical solution for this case, insofar as the integral power losses are concerned. For the other two cases, however, the coarse mesh tended to overpredict the losses, but as the grid was refined the numerical solutions clearly converged toward a grid insensitive solution, which was in good agreement with the measurements. Mesh independency is also verified for primitive flow variables. A typical convergence with mesh refinement for velocity is plotted in Fig. 5. These results show that the two finest meshes yield very similar results, suggesting that the computed solution is insensitive to further mesh refinement.

As seen in Fig. 4, for the highest cardiac output (3 l/min) condition the numerical simulations agreed well with the measurements only within a relatively narrow band of flow splits. This discrepancy should be attributed to the fact that for this condition transition to turbulence becomes very likely within the pulmonary arteries. Based on the vessel hydraulic diameter, the Reynolds number calculated for both pulmonary arteries is close to 2300 for most of the pulmonary flow split range. The SVC flow, on the other hand, turned out to be relatively noncritical as compared to the PAs. For example, at 3 l/min, 60/40 IVC/SVC split, the SVC Reynolds number reaches 1900. Operating conditions corresponding to turbulent flow are shown with dashed lines in the hydrodynamic power loss map of Fig. 4. Since all numerical simulations in this work assumed laminar flow, it is not surprising that the predicted power losses began to deviate substantially from the measurements for conditions in the turbulent flow regime. Work is currently underway to carry out turbulent flow calculations using a traditional steady RANS model and other more advanced unsteady statistical turbulence models. These results, however, will be reported in future communications.

Mean Velocity Field

In this section we compare the calculated flow fields with the time-averaged velocity magnitude measurements obtained with DPIV. As we have previously mentioned, both the DPIV experiments and flow visualizations revealed a complex, unsteady flow for all cases considered in this work (see subsequent section for a detailed discussion of the

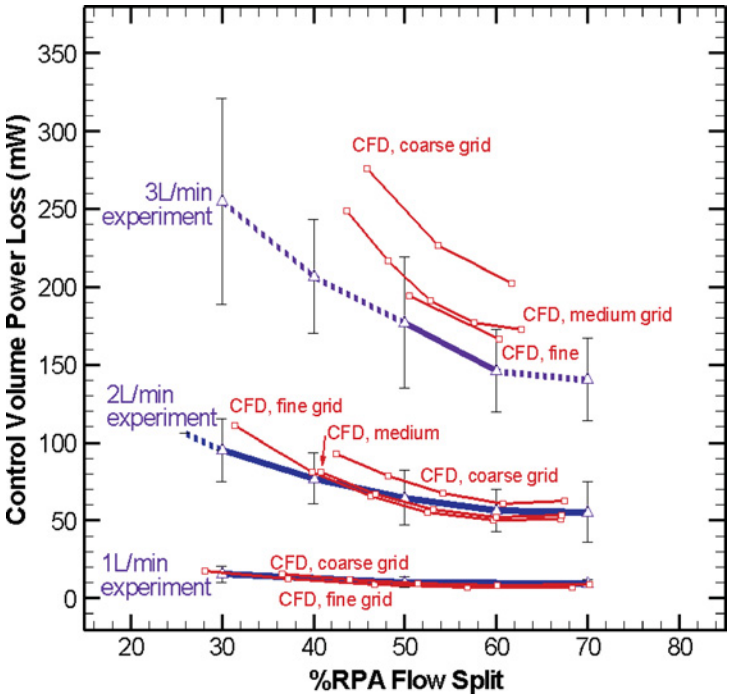

FIGURE 4. Grid size verification and experimental comparison of the steady-laminar CFD model. Dashed lines denote conditions where Re_{LPA} or Re_{RPA} > 2300, i.e., flow should be fully turbulent at one of the pulmonary arteries.

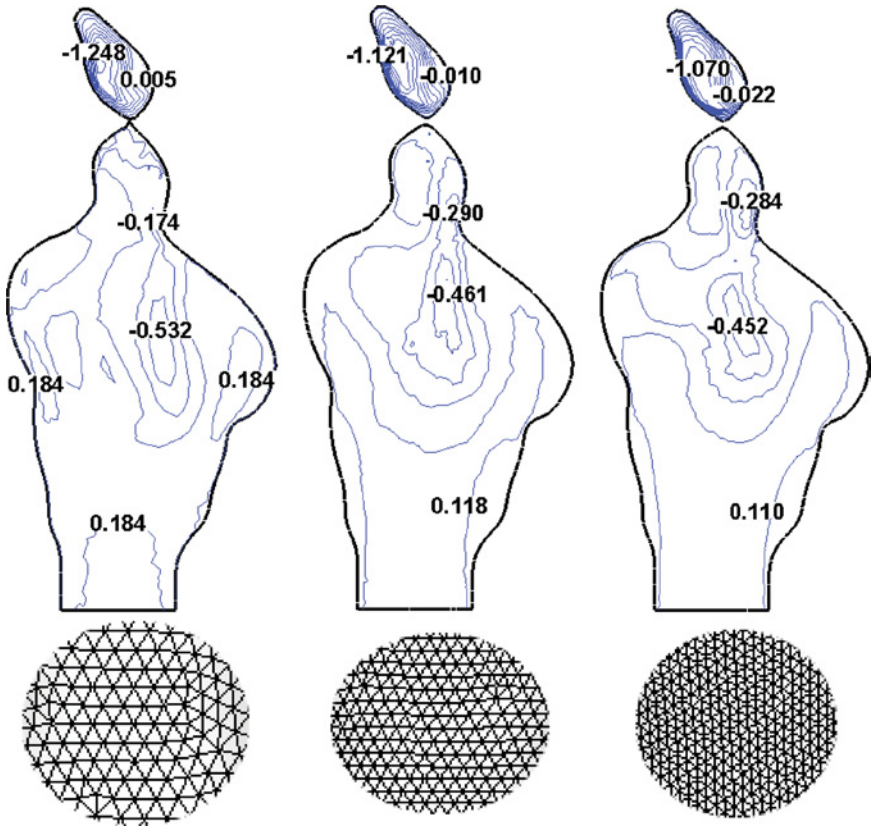

FIGURE 5. Typical grid convergence of the velocity field for Case 23. Axial velocity component contours (m/s) are plotted in a typical coronal plane for different unstructured grid refinements (Numbers of tetrahedral elements used are 64836 (coarse), 147721 (medium) and 340315 (fine), left-to-right).

instantaneous flow fields). To construct the time-averaged fields, instantaneous PIV measurements were collected and averaged over 300 frames. For the FIDAP computations no averaging was needed since, as previously discussed, only steady-state results have been obtained in this work. For the in-house code, however, instantaneous flow fields were averaged over a time interval comparable to that used in the PIV experiments.

During the numerical verification studies, the velocity profile of inflow boundary conditions was found to have a strong effect on the calculated flow field; for comparison, plug and fully developed flow were specified at the SVC and IVC boundaries. While both profiles have the same average flowrate, they resulted in significantly different flow fields within the TCPC. Specifying a plug flow velocity distribution at the IVC or SVC may be a practical CFD modeling option, especially for anatomical flows with arbitrary vessel shape and orientation, but it introduces considerably less vorticity into the flow as compared to the parabolic fully developed profile. Inflow vorticity is redistributed via vortex skewing and intensified via stretching, and thus, its intensity could greatly affect the strength and structure of secondary flow and the distribution of momentum throughout the connection region. All subsequently reported results have been obtained using fully developed inlet profiles, which is also the experimental condition, likewise this boundary condition yielded results in close agreement with the measurements.

The time-averaged DPIV measurements of velocity magnitude for Case 13 are compared with the steady-state FIDAP results and the time-averaged results obtained with the in-house code in Fig. 6. The imaging planes are labeled from the most anterior (a) to the most posterior (d). It is important to point out that unpolished interior model surfaces introduced a background noise effect on PIV cross correlation, which resulted in systematically lower velocity magnitudes than CFD (max 15%) for slices farther away from the PIV camera. The experimental results reveal that the SVC flow exits the vein as a high velocity jet and dives down into the IVC along the left anterior wall before going back up along the right anterior wall, Fig. 6(a). The IVC flow becomes more dominant towards the posterior side. Along the posterior wall, Fig. 6(d), the flow is completely governed by the IVC stream. The intermediate planes that are shown in Figs. 6(b) and 6(c) exhibit the recirculation pattern throughout the pouch, as well as the flow separation in the SVC. Both CFD predictions appear to capture most of these experimental trends with reasonable accuracy. This level of agreement is indeed remarkable if one takes into account the complexity of the flow and the fact that the two numerical results were obtained using entirely different numerical methodologies and grid structures.

The results shown in this section clearly demonstrate that if only time-averaged flow quantities are of interest either FIDAP or the in-house code would be sufficient to obtain results of reasonable engineering accuracy. In fact, FIDAP would be the model of choice for this case since its first-order accuracy allows for higher cardiac outputs and for steady-state solution to be obtained at only a fraction of the time required to obtain results with the unsteady, in-house flow solver. However, this conclusion is drastically altered when we focus attention on the unsteady characteristics of the flow.

Instantaneous Flow

Flow visualization underscored the enormous complexity of the flow in the anatomical TCPC even for flow rates well within the laminar flow regime (*Re* 300–800, 1 l/min total cardiac output). Figure 7 displays several snapshots from the flow visualization experiments and the unsteady numerical simulations with the in-house code (visualized in terms of instantaneous streamlines). Instantaneous streamlines are generated using Tecplot CFD Analyzer 3.0 from the transient numerical solution sets which are assigned to different zones. Particles are released at the positions close to where the dye was released in the experiments. To better appreciate the complexity and dynamical nature of the flow in this region, a complete video recording from the flow visualization experiment at different flow conditions is prepared.[50] Figure 7 clearly shows complex, rotational flow patterns and intense flow unsteadiness in the connection region. In both the experiments and the numerical simulations this complex unsteady flow emerged naturally, without any imposed external forcing other than ambient laboratory disturbances present in any experiment and numerical disturbances due to truncation and other discretization errors, respectively. The onset appears to be the result of flow instability at the saddle point in the center of the connection where the IVC and SVC collide and divide laterally into the LPA and RPA. The instability manifests itself in the form of seemingly random meandering of the flow as shown in the three representative snapshots shown in Fig. 7. There are instants in time during which IVC flow from the anterior side enters the connection region, recirculates, and exits almost exclusively through the LPA as in Fig. 7(a). At other moments, however, flow from the same region is almost equally divided within the LPA and RPA, Fig. 7(b), or enters the RPA in its entirety, Fig. 7(c). Although not pictured here, similar chaotic meandering is observed for the SVC flow as well as for flow originating from other regions within the IVC and SVC. At most instants in time the flow entering the connection region from either the IVC or SVC is seen to recirculate in a very complex and highly three-dimensional manner before it is diverted towards the pulmonary branches. Similar instabilities have also been stated by Khunatorn *et al.*[38] as a possible cause for the mismatch in their CFD and PIV results. Bolzon *et al.*[3] numerically calculated the onset of instability to be at $Re = 1100$ for their larger (SVC and IVC dia. = 11.2 mm) idealized model with caval offset. Here, the extra volume of the pouch set up

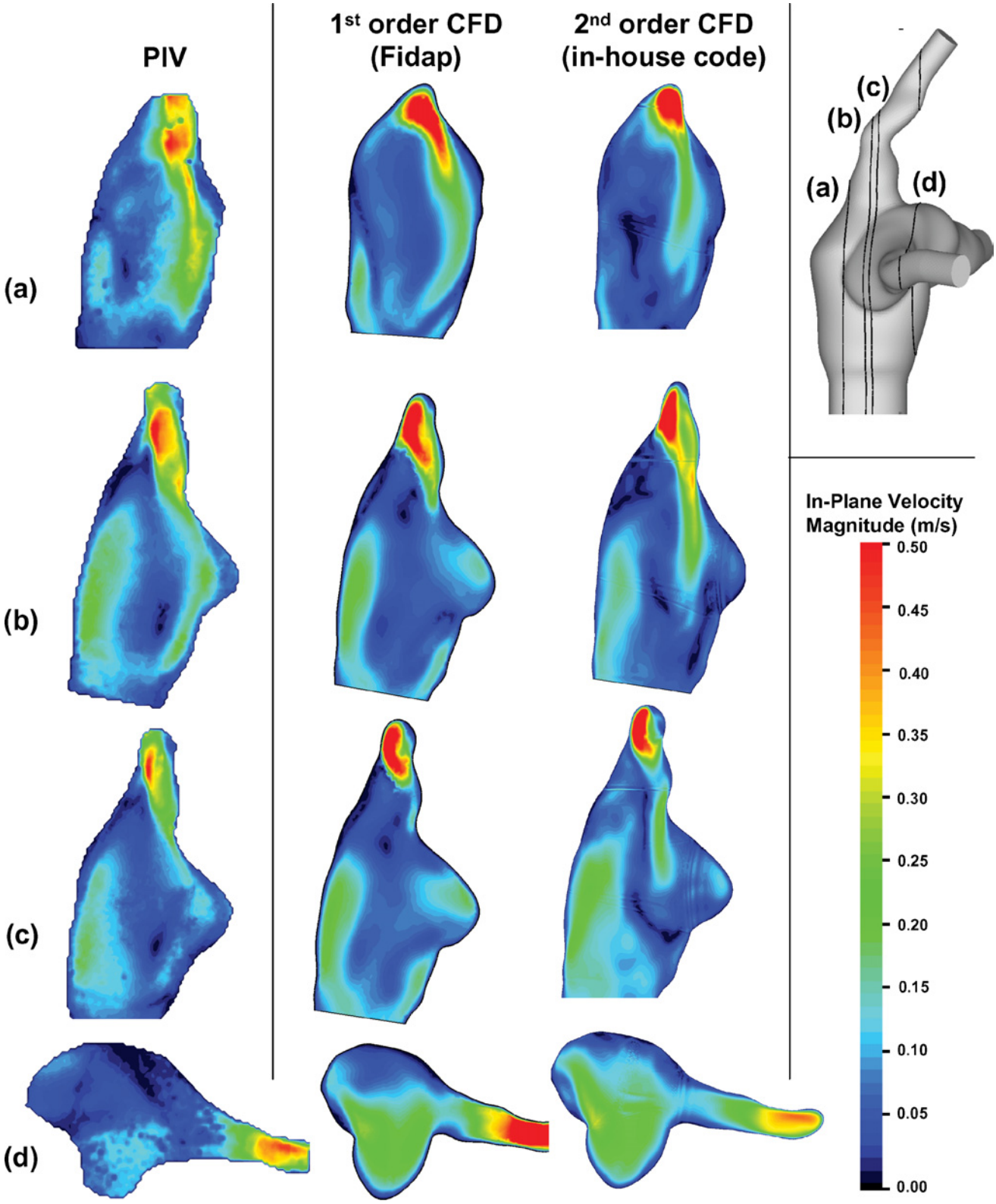

FIGURE 6. Quantitative assessment of the flow field using PIV, CFD first (with fine grid size) and second order accurate at 1 l/min; inflow split: 60/40 IVC/SVC; outflow split: 50/50 LPA/RPA, Case 13. Imaged planes are indexed from the most anterior (a) to the most posterior (d). Slice locations are displayed on the upper-right diagram.

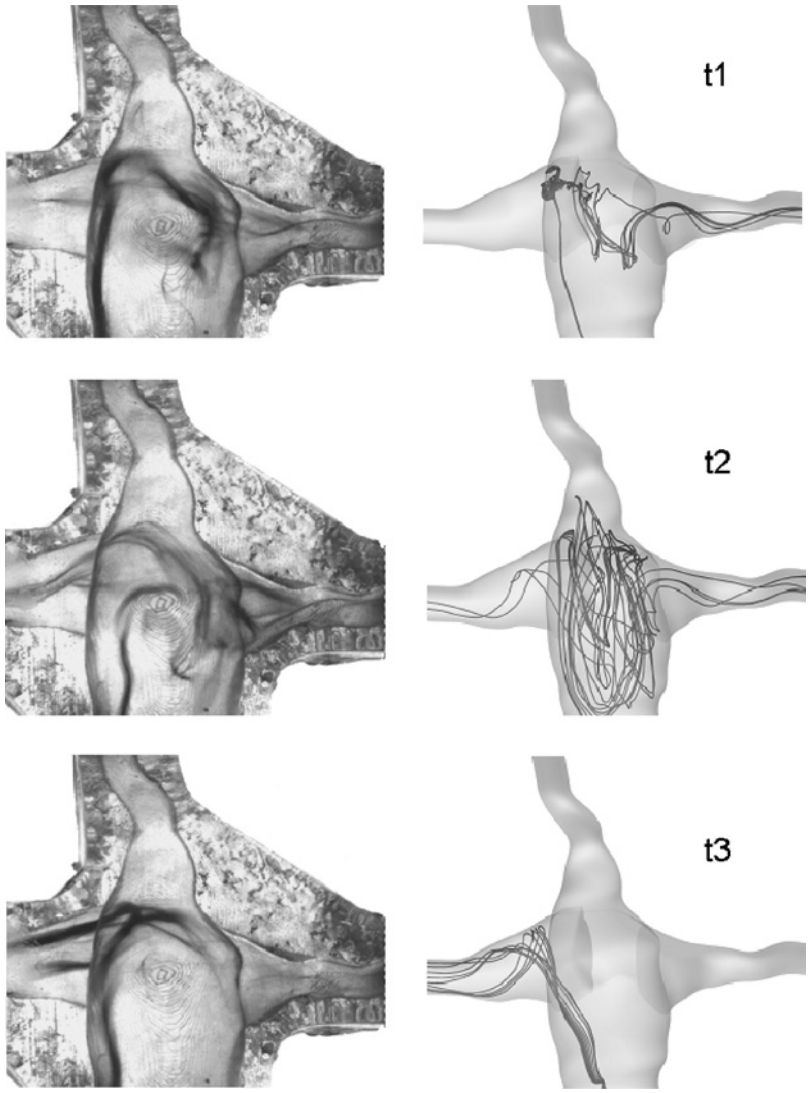

FIGURE 7. At 1 l/min, flow visualization (Left) showed that the TCPC flow was dominated by complex, unsteady, and highly 3D flow structures. Using higher-order accuracy transient simulations those were also captured in CFD (Right); Case 13, at progressing time instances (t1, t2, t3). For the numerical solution instantaneous streamlines are plotted.

an additional spatial degree of freedom, thus allowing the flow instability to become clearly visible and prevail for all flow conditions. In our work, we also find that essentially the same instability mode exists for all cases considered with both the frequency and overall complexity of the flow increasing with increasing branch Reynolds numbers.

As seen in Fig. 7, the numerical simulations capture all these complex flow patterns with reasonable similarity. This finding is particularly encouraging since the mean-flow comparisons shown in the previous section established that the simulated unsteady flow is in good qualitative agreement with the measured time-averaged flow. It should be pointed out, however, that a more comprehensive validation of the in-house code is required in so far as the unsteady features of the flow is concerned. Quantitative comparisons need to be made for the spectral content of the simulated and measured flow (temporal frequencies of the flow) and the intensity of unsteadiness (Reynolds stresses). This validation, however, will require highly resolved unsteady measurements, which due to current limitations in our DPIV instrumentation are not possible. The dominant frequency of the oscillations as observed in flow visualizations (11.1 ± 1.25 Hz, based on four independent observers and two major flow events at 1 l/min), and CFD calculations ($\sim$10 Hz, major frequency) were of the same order as the data acquisition capability of our standard DPIV setup. Work is currently under way to address these difficulties and the results will be reported in a future publication. The preliminary numerical simulations shown in Fig. 7 will help guide and design these experiments.

Because of the highly three-dimensional nature of the flow, it is very difficult to convey its complete structure with

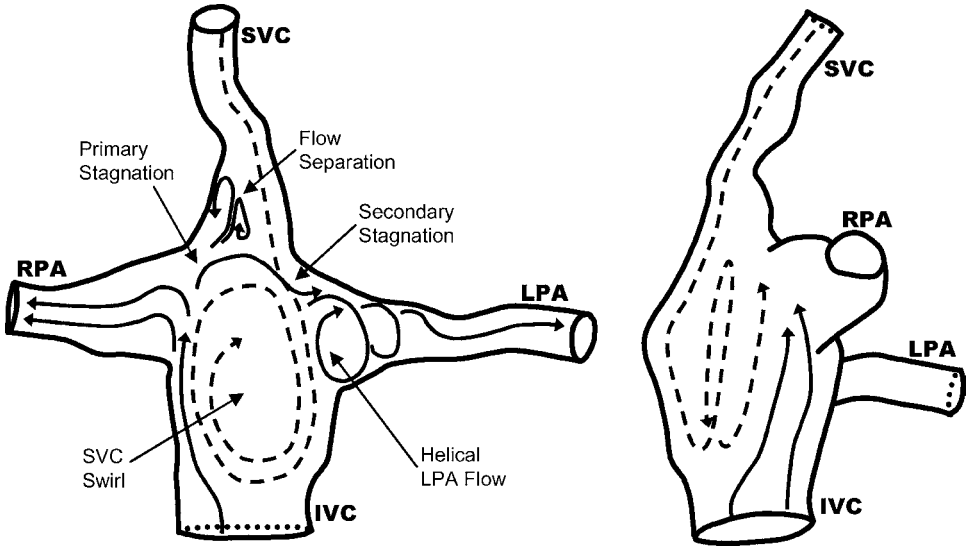

FIGURE 8. Schematic of the flow structure in the anatomical intra-atrial model as it was observed in flow visualization when watching from the anterior side (Left figure) or from the right side (Right figure). Flow that emanates from SVC is represented with the dotted lines. Major flow structures are indicated with arrows.

a few instantaneous snapshots or video animations viewed from one particular angle. For this reason we analyzed both the laboratory observations and numerical flow fields from different angles and compiled the main flow features in the sketches shown in Fig. 8. Close to the anastomosis location, the SVC bends from the posterior to anterior side and becomes wider. This divergent geometrical configuration resulted in a flow separation region with fast flow on one side and slow recirculating flow on the other. Interestingly, coming all the way back up towards the SVC, IVC flow is occasionally observed to reside in this recirculation region. In the same fashion as the SVC, the IVC became wider towards the anastomosis creating a large pouch. An IVC flow recirculation could thus have been expected at the opening of the IVC. Instead, there was the overriding SVC stream, swirling clockwise along the anterior wall. This was believed to be a combined effect of the SVC and IVC geometries. Because of a smaller vessel diameter, the SVC stream was 5 to 6 times faster than that from the IVC. Moreover, the SVC was oriented towards the anterior side, where the IVC became wider. The combination of these geometric features created very little resistance from the IVC stream against the SVC flow. The SVC flow thus recirculated deep down into the IVC. Due to the complex geometry, in addition to the primary stagnation/shear surface at the mean PA level, a secondary stagnation/shear region was observed. It appeared at the end of the full turn of the recirculating SVC flow and was located at the RPA inlet proximal to the SVC.

To further illustrate the structure of the three-dimensional vortices in the connection region, we show in Fig. 9 a snapshot of two calculated iso-surfaces of normalized helicity, which is the cosine of the angle between the vorticity and velocity vectors. Normalized helicity is a very effective tool for elucidating the structure of coherent vortices in the flow as by definition it attains maximum magnitude in regions where the velocity and vorticity vectors are aligned. As seen in Fig. 9, very complex vortical structures occupy all branches and the connection region. Well defined streamwise vortices exist in the LPA and RPA, and are induced by the lateral skewing of incoming vorticity by the complex flow in the connection region. The helicity iso-surfaces, further shows intense spiraling of the

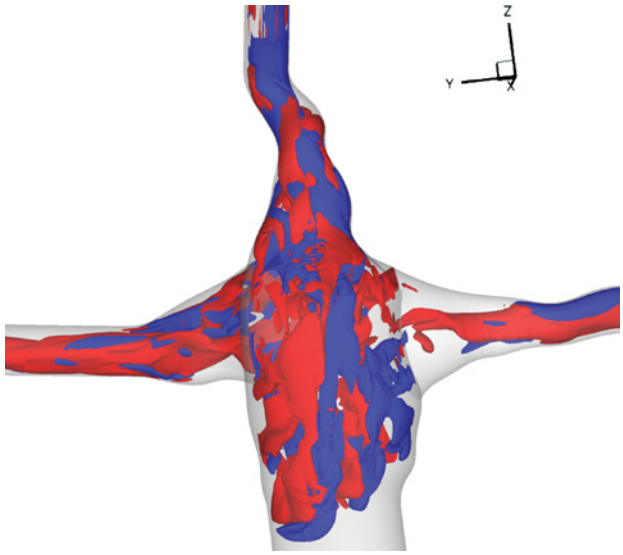

FIGURE 9. Iso-surface plot of instantaneous helicity surfaces originating from the SVC, for Case 13. This snap shot of the in-house computation at 1 l/min, further illustrates the important recirculation that takes place in the pouch.

streamwise structures in the LPA and RPA and the generation of complex, small scale structures in the connection region.

DISCUSSION

CFD verification and validation[21,7] is an important requirement for the TCPC research, as well as for all applications of computational cardiovascular fluid dynamics. Particularly, these requirements should not be ignored in clinical CFD applications that involve patients. This is even more critical when CFD is aimed at surgical planning. Likewise, physicians and surgeons who may plan on applying any computer generated result or act as end users of a clinical CFD tool, should be aware of CFD validation concepts[52,26] and the possible numerical uncertainties. CFD is a breakthrough in medicine that, like any tool, is valuable when applied in the correct way.

For any unexplored anatomic morphology, most of the flow features and underlying flow physics will be an unknown, at the beginning of the numerical modeling effort. An illustration is provided in this study for the anatomical TCPC flows which turn out to be intrinsically transient and transitional. In these cases, a combined experimental and computational approach is essential and requires a balanced emphasis on the research resources in order to avoid jumping to the most complex computational model before sorting out the fundamental concerns. As demonstrated in this study each step of the numerical modeling sophistication has its own advantages.

The fluid dynamic instability, as described here, is exacerbated by the large connection area. For other morphologies that are closer in shape to the idealized models, having more uniform conduit sizes and with caval offset, less flow instability is expected and when present occurs at higher Reynolds numbers (Bolzon *et al.*[3] estimated the frequency to be 2.56–3.45 Hz, at $Re = 1600$, based on average PA flow for their idealized model with no caval offset. This frequency is in the same order as our anatomic case: $\sim$10 Hz at $Re_{\mathrm{PA}} = 670$). Likewise, a global instability index would be useful to compare different TCPC geometries. Clinically high levels of flow instabilities would severely increase the hydrodynamic power loss; while on the other hand, they will contribute to beneficial hepatic blood mixing. As the total cardiac output increases, Reynolds numbers and the frequency of the fluctuations increase. This may signal the onset of transition to turbulence. Such a conclusion is consistent and correlate well with increasing experimental standard deviations and differences between steady, laminar first-order, CFD, and *in vitro* benchtop data as summarized in Fig. 4.

The experimental model was manufactured using stereolithography so as to be the exact replica of the computational one. Transparent resins proved to be practical for flow visualization and digital particle velocimetry experiments. In this methodology, the inner surfaces of the experimental model were left "as is" with no interior polishing, so as not to accidentally alter the anatomy. This decision affected the optical quality of the experimental model. Although useful PIV data was acquired, the observed velocity values were systematically lower for the slices that were further away from the PIV camera. Slight light scattering was observed throughout the model. Fluorescent particles, color filters, and background noise filtering were used to improve the PIV image quality. In general CFD solutions showed more complex flow features than PIV, due to data averaging in PIV along finite size interrogation windows. The highest velocity regions observed in the numerical solutions were smaller than the interrogation window size for PIV. Furthermore, these peaks were located close to the SVC wall and, would not be captured by the PIV reasonably well, due to partial volume effects, unless special techniques are employed.[2] For the examined TCPC model, the order of difference in the velocity magnitudes at the IVC and SVC caused limitations in finding an optimal laser pulse spacing applicable to the entire field. Additionally, the best possible laser thickness of $\sim$0.5 mm was comparable to the height of the anterior model span which was $\sim$18 mm. This large measurement volume, relative to the size of our anatomical model, further smoothed out the experimental measurements in the anterior direction.

Complete hydrodynamic performance evaluation of the TCPC requires additional parameters including IVC/SVC contributions to LPA and RPA flow, residence times of IVC and SVC streams, connection shear and pressure maps, dissipation field,[29,17,10] and individual branch and connection pressure drop contributions. As the anatomic sizes and morphologies can be highly variable in the TCPC, comparative analysis may require that performance parameters be scaled. Additionally, transient flow in the TCPC necessitates the calculation of exact unsteady analogs of these parameters, instead of practical time averages of the steady definitions.[45] A validated CFD model is a first step for the accurate calculation of these clinically important parameters.

In this study, the steady inflow boundary conditions at SVC and IVC are used mainly to concentrate on the intrinsic flow instability effects. Apparently, any inflow pulsatility will significantly augment the complexity presented here. Since no MRI flow data were available for this particular TCPC anatomy, and since our region of interest is located further down the venous side, flow at SVC and IVC branches is assumed to be steady. The actual mechanism of upstream pulsatility, if severe, involves breathing effects, TCPC template type, vessel compliance, systemic pulsatility and if exist the effects of fenestration.

For our TCPC problem, second order accuracy is demonstrated to be critical for valid CFD results. Most of the commercial packages, including FIDAP provide schemes

that are formally accurate. However, the most critical problem we have encountered in this application stems from the need to find a code that handles the complex TCPC geometry with second-order accuracy. Available commercial codes either use unstructured grids, with finite-volume or finite-element techniques, or multiblock methods with patched grids. The former approach (such as that used in FIDAP) can handle the complex geometry but it is well known in the literature that it is very difficult to obtain second-order accuracy on unstructured meshes regardless of whether a finite element or a finite volume method is used.[51,67] The latter approach could be formulated in conjunction with second-order accurate numerics (several such commercial codes exist) but unfortunately it can not handle geometries as complex as a typical TCPC anatomy. Recall that the in-house multiblock code uses Chimera overset meshes (i.e. blocks that are arbitrarily overlapping with each other), which is the only feasible approach for handling complex geometries with block-structured meshes.

Studies with the in-house code are performed starting with a significantly finer grid resolution than the finest mesh resolution we used with FIDAP. No further grid refinement studies were considered for the in-house code as the grid we employed could capture most experimental trends with reasonable accuracy. This not withstanding, however, careful mesh and time step sensitivity studies are important for the investigation of the flow physics on this TCPC setting. Numerical sensitivity studies along with more comprehensive validation of the in-house code (detail comparison of velocity distribution, statistics of flow unsteadiness, etc.) and further investigation of the flow physics are currently under way and will be reported in future communications.

In this study, we have focused solely on the CFD validation issues for a given anatomic reconstruction. The reconstruction process, leading from the patient MRI data to a CAD file for CFD grid generation is still a long and tedious task with repeated approximations, that might jeopardize the ultimate accuracy of the model. This is of prime importance for the physiological relevance of any numerical study to the cardiovascular field, especially in TCPC flows, where the efficiency of the connection has been shown to be highly dependent on the geometry.[53] Thus, utmost care should be taken when reconstructing and designing the model. Some of the unique accuracy and uncertainty issues have already been highlighted in literature,[1,47,61] as a research area of their own. Reverse engineering and stereolithographic techniques are very useful for quantifying these errors. In our case, the experimental and CFD geometries laid within 0.1 mm of each other, due to the optimal accuracy of our stereolithographic hardware. The differences between the reconstructed geometry and the true anatomy are more difficult to assess and are further discussed in detail by Frakes *et al.*[16]

CONCLUSIONS

At the start of this study, flow physics and detailed flow field characteristics were virtually unknown for the selected TCPC anatomy. All available information was extrapolative in nature, arising from earlier studies on idealized geometries and qualitative hemodynamic image data from other morphologies. For this setting, a combined CFD and experimental *in vitro* modeling approach has been demonstrated to be essential. Even though the encountered TCPC flow appeared to be far more complex than expected and difficult to simulate numerically due to its highly unsteady character, we showed that careful CFD modeling can indeed yield results that are in good agreement with experiments, both in global quantities like power loss and in velocity fields. Frequency of flow instability estimated from time-accurate calculations was also good agreement with experiments.

This study indicated that the "control volume power loss" parameter may still be calculated with good accuracy, at least for conditions in the laminar flow regime, using a commercially available, first-order steady state CFD model. These steady state solutions are not as computationally demanding as the high resolution time-accurate calculations. Therefore, a quick overall assessment of hydrodynamic performance in the TCPC anatomy is clinically possible. Our work clearly shows, however, that good experimental agreement in the global control volume results should not imply that the detailed flow field is accurately captured. In our case, attempts to simulate the unsteady flow structures with the first-order accurate commercial code FIDAP were inconclusive and complete characterization of the highly three-dimensional and unsteady flow structures was made possible only after careful numerical modeling with a second-order accurate in-house flow solver on a very fine computational mesh. Such sophisticated modeling currently requires weeks of computational time. This excessive computational overhead can be drastically reduced (from weeks to several hours), however, by optimizing the code to take advantage of massively parallel computational platforms, which are becoming increasingly more affordable and widespread. It is, thus, reasonable to conclude that in the near future such advanced CFD modeling techniques will evolve into practical tools for surgical planning.

ACKNOWLEDGMENTS

This work was supported by a grant from the National Heart, Lung, and Blood Institute, HL67622. The Stereolithograpic model parts are manufactured by Steven Sheffield, Rapid Prototyping and Manufacturing Institute, Georgia Institute of Technology, Atlanta, GA.

REFERENCES

[1]August, A. D., D. C. Barratt, A. D. Hughes, F. P. Glor, T. SAMcG, and X. Y. Xu. Accuracy and reproducibility of CFD

predicted wall shear stress using 3D ultrasound images. *J. Biomech. Eng.* 125:218–22, 2003.
[2]Bale-Glickman, J., K. Selby, D. Saloner, and Ö. Savas. Experimental flow studies in exact-replica phantoms of atherosclerotic carotid bifurcations under steady input conditions. *J. Biomech. Eng.* 125:38-48, 2003.
[3]Bolzon, G., G. Pedrizzetti, M. Grigioni, L. Zovatto, C. Daniele, and G. D'Avenio. Flow on the symmetry plane of a total cavopulmonary connection, *J. Biomech.* 35:595–608, 2002.
[4]Cebral, J. R., P. J. Yim, R. Lo, O. Soto, and P. L. Choyke. Blood flow modeling in carotid arteries with computational fluid dynamics and MR imaging. *Acad. Radiol.* 9:1286–1299, 2002.
[5]Celik, I., C. J. Chen, P. J. Roache, and G. Scheuerer (editors). Symposium on quantification of uncertainty in computational fluid dynamics. In: Proceedings of ASME Fluids Engineering Division, Washington, DC, 1993.
[6]Cochrane, A. D., C. P. Brizard, D. J. Penny, S. Johansson, J. V. Comas, T. Malm, and T. R. Karl. Management of the univentricular connection: are we improving? *Eur. J. Cardiothorac. Surg.* 12:107–115, 1997.
[7]Coleman, H. W. Some observations on uncertainties and the verification and validation of a simulation. *J. Fluids Eng.* 125:733–735, 2003.
[8]de Laval, M. R., P. Kilner, M. Gewillig, and C. Bull. Total cavopulmonary connection: A logical alternative to atriopulmonary connection for complex Fontan operations. Experimental studies and early clinical experience. *J. Thorac. Cardiovasc. Surg.* 96:682–695, 1988.
[9]DeGroff, C. G., B. L. Thornburg, J. O. Pentecost, K. L. Thornburg, M. Gharib, D. J. Sahn, and A. Babtista. Flow in the early embryonic human heart: A numerical study. *Pediatr. Cardiol.* 24:375–380, 2003.
[10]Ensley, A. E., A. Ramuzat, T. M. Healy, G. P. Chatzimavroudis, C. Lucas, S. Sharma, R. Pettigrew, and A. P. Yoganathan. Fluid mechanic assessment of the total cavopulmonary connection using magnetic resonance phase velocity mapping and digital particle image velocimetry. *Ann. Biomed. Eng.* 28:1172–1183, 2000.
[11]Ensley, A. E., P. Lynch, G. P. Chatzimavroudis, C. Lucas, S. Sharma, and A. P. Yoganathan. Toward designing the optimal total cavopulmonary connection: An *in vitro* study. *Ann. Thorac. Surg.* 68:1384–1390, 1999.
[12]Farhat, C., S. Lanteri, and H. D. Simon. TOP/DOMEC A software tool for mesh partitioning and parallel processing. *J. Comput. Sys. Eng.* 6:13–26, 1995.
[13]Fogel, M. A., A. Hubbard, and P. M. Weinberg. A simplified approach for assessment of intercardiac baffles and extracardiac conduits in congenital heart surgery with two- and three-dimensional magnetic resonance imaging. *Am. Heart J.* 142(6):1028–1036, 2001.
[14]Fogel, M. A., P. M. Weinberg, J. Rychik, A. Hubbard, M. Jacobs, T. L. Spray, and J. Haselgrove. Caval contribution to flow in the branch pulmonary arteries of Fontan patients with a novel application of magnetic resonance presaturation pulse. *Circulation* 99:1215–1221, 1999.
[15]Formaggia, L., F. Nobile, A. Quarteroni, and A. Veneziani. Multiscale modelling of the circulatory system: A preliminary analysis. *Comput. Visual Sci.* 2:75–83, 1999.
[16]Frakes, D., C. Conrad, T. Healy, J. Monaco, M. Smith, M. Fogel, S. Sharma, and A. P. Yoganathan. Application of an adaptive control grid interpolation technique to morphological vascular reconstruction. *IEEE Trans. Bio. Eng.* 50(2):197–206, 2003.
[17]Frakes, D., M. Smith, D. de Zélicourt, K. Pekkan, A. Yoganathan. Three-dimensional velocity field reconstruction. *J. Biomech. Eng.* 126(6):727–735, 2004.
[18]Frakes, D., M. Fogel, J. Parks, S. Sharma, M. J. T. Smith, and A. P. Yoganathan. MRI-based 3D modeling of cardiac vascular anatomies for surgical applications. In: Proceedings of the American College of Cardiology Annual Scientific Session 2004, New Orleans, LA, March 2004.
[19]Freitas, C. J. Journal of fluids engineering editorial policy statement on the control of numerical accuracy. *J. Fluids Eng.* 115:339–340, 1993.
[20]Freitas, C. J. Perspective: Selected benchmarks from commercial CFD codes. *J. Fluids Eng.* 117(2):208–218, 1995.
[21]Freitas, C. J. The issue of numerical uncertainty. *Appl. Math. Model.* 26:237–248, 2002.
[22]Friesen, C. L. H., and J. M. Forbess. Surgical management of the single ventricle. *Prog Pediatr. Cardiol.* 16:47–68, 2002.
[23]Ge, L., S. C. Jones, F. Sotiropoulos, T. M. Healy, and A. P. Yoganathan. Numerical simulation of flow in mechanical heart valves: Grid resolution and the assumption of flow symmetry. *J. Biomech. Eng.* 125(5):709–718, 2003.
[24]Geva, T., D. J. Sahn, and A. J. Powell. Magnetic resonance imaging of congenital heart disease in adults. *Prog. Pediatr. Cardiol.* 17:21–39, 2003.
[25]Guadagni, G., E. L. Bove, F. Migliavacca, and G. Dubini. Effects of pulmonary afterload on the hemodynamics after the hemi-Fontan procedure. *Med. Eng. Phys.* 23:293–298, 2001.
[26]Guide for the Verification and Validation of Computational Fluid Dynamics Simulations. American Institute of Aeronautics and Astronautics (AIAA), 1998, G-077-1998.
[27]Haas, G. S., H. Hess, M. Black, J. Onnasch, F. W. Mohr, and J. A. M. van Son. Extracardiac conduit Fontan procedure: Early and intermediate results. *Eur. J. Cardiothorac. Surg.* 17:648–654, 2000.
[28]Haroutunian, V., M. S. Engelman, and I. Hasbani. Segregated finite element algorithms for the numerical solution of large-scale incompressible flow problems. *Int. J. Numer. Methods Fluids* 17:323–348, 1993.
[29]Healy, T. M., C. Lucas, and A. P. Yoganathan. Noninvasive fluid dynamic power loss assessments for total cavopulmonary connections using the viscous dissipation function: A feasibility study. *J. Biomech. Eng.* 123:317–324, 2001.
[30]Hjortdal, V. E., K. Emmertsen, E. Stenbog, T. Frund, M. R. Schmidt, O. Kromann, K. Sorensen, and E. M. Pedersen. Effects of exercise and respiration on blood flow in total cavopulmonary connection. A real-time magnetic resonance flow study. *Circulation* 108:1227–1231, 2003.
[31]Hughes, T. R. J., and A. N. Brooks. A multidimensional upwind scheme with no crosswind diffusion. In: Finite Element Methods for Convection Dominated Flows, edited by T. J. R. Hughes. ASME Press, New York, 1979, pp. 19–35.
[32]Hughes, T. R. J., L. P. Franca, and M. Becestra. A new finite element formulation for computational fluid dynamics, V. Circumventing the Babuska-Brezzi conduction, A stable Petrov-Galerkin formulation of the Stokes problem accommodating equal-order interpolations. *Comp. Meth. Appl. Mech. Eng.* 59:85–99, 1986.
[33]California Institute of Technology. In: Proceedings of the International Biofluid Mechanics Conference, organized by S. Einav, R. Ethier, M. Gharib, R. Kamm, D. Liepsch, and A. P. Yoganathan. California Institute of Technology, December 12–14, 2003.
[34]Iordanis, C., V. D. Butty, V. B. Makhijani, D. Poulikakos, and Y. Ventikos. Pulsatile blood flow in anatomically accurate vessels with multiple aneurysms: A medical intervention planning application of computational haemodynamics. *Flow Turbul. Combust.* 71:333–346, 2003.
[35]Jacobs, P. Stereolithography and Other RP&M Technologies. ASME Press, New York, 1996.

[36]Johnston, B. M., P. R. Johnston, S. Corney, and D. Kilpatrick. Non-Newtonian blood flow in human right coronary arteries: Steady state simulations. *J. Biomech.* 37(5):709–720, 2004.

[37]Karypis, G., and V. Kumar. MeTIS—A Software Package for Partitioning Unstructured Graphs, Partitioning Meshes and Computing Fill-Reducing Orderings of Sparse Matrices (Version 3.0). Minnesota: University of Minnesota, Department of Computer Science/Army HPC research center, October 1997.

[38]Khunatron, Y., R. Shandas, C. DeGroff, and S. Mahalingam. Comparison of *in vitro* velocity measurements in a scaled total cavopulmonary connection with computational predictions. *Ann. Biomed. Eng.* 31:810–822, 2003.

[39]Kim, Y. H., P. G. Walker, A. A. Fontaine, S. Panchal, A. E. Ensley, J. Oshinski, S. Sharma, B. Ha, C. L. Lucas, and A. P. Yoganathan. Hemodynamics of the Fontan connection: An *in vitro* study. *J. Biomech. Eng.* 117:423–428, 1995.

[40]Ku, J. P., M. T. Draney, F. R. Arko, W. A. Lee, F. P. Chan, N. J. Pelc, C. K. Zarins, and C. A. Taylor. *In vivo* validation of numerical prediction of blood flow in arterial bypass grafts. *Ann. Biomed. Eng.* 30:743–752, 2002.

[41]Laccarino, G. Predictions of a turbulent separated flow using commercial CFD codes. *J. Fluids Eng.* 123:819–828, 2001.

[42]Liu, Y., K. Pekkan, S. C. Jones, and A. P. Yoganathan. The effects of different mesh generation methods on fluid dynamic analysis and power loss in total cavopulmonary connection (TCPC). *J. Biomech. Eng.* 126(5):594–603, 2004.

[43]Masters, J. C., M. Ketner, M. S. Bleiweis, M. Mill, A. P. Yoganathan, and C. L. Lucas. The effect of incorporating vessel compliance in a computational model of blood flow in a total cavopulmonary connection (TCPC) with caval offset. *J. Biomech. Eng.* 2002.

[44]Metcalfe, R. W. The promise of computational fluid dynamics as a tool for delineating therapeutic options in the treatment of aneurysms. *AJNR Am. J. Neuroradiol.* 24:553–554, 2003.

[45]Migliavacca, F., G. Dubini, E. L. Bove, and M. R. de Leval. Computational fluid dynamics simulations in realistic 3-D geometries of the total cavopulmonary anastomosis: The influence of the inferior caval anastomosis. *J. Biomech. Eng.* 125:805–813, 2003.

[46]Migliavacca, F., P. J. Kilner, G. Pennati, G. Dubini, R. Pietrabissa, R. Fumero, and M. R. de Leval. Computational fluid dynamic and magnetic resonance analyses of flow distribution between the lungs after total cavopulmonary connection. *IEEE Trans. Bio. Eng.* 46(4):393–399, 1999.

[47]Moore, J. A., D. A. Steinman, S. Prakash, K. W. Johnston, and C. R. Either. A numerical study of blood flow patterns in anatomically realistic and simplified end-to-side anastomoses. *J. Biomech. Eng.* 121:265–272, 1999.

[48]Nowak, N., P. P. Kakade, and A. V. Annapragada. Computational fluid dynamics simulation of airflow and aerosol deposition in human lungs. *Ann. Biomed. Eng.* 31:374–390, 2003.

[49]Oshima, M., R. Torii, T. Kobayashi, N. Taniguchi, and K. Takagi. Finite element simulation of blood flow in the cerebral artery. *Comput. Methods Appl. Mech. Eng.* 191:661–671, 2001.

[50]Pekkan, K., D. A. de Zélicourt, and A. P. Yoganathan. *In vitro* flow visualization of a post-surgery total cavopulmonary connection anatomy, 21st Annual Gallery of Fluid Motion (movie). In: Proceedings of the Applied Physical Society Division of Fluid Dynamics 56th Annual Meeting, 2003.

[51]Perot, B. Conservation properties of unstructured staggered mesh schemes. *J. Comput. Phys.* 159(1):58–59, 2000.

[52]Roache, P. J. Verification and Validation in Computational Science and Engineering. Albuquerque, New Mexico: Hermosa publishers, 1998.

[53]Ryu, K., T. M. Healy, A. E. Ensley, S. Sharma, C. L. Lucas, and A. P. Yoganathan. Importance of accurate geometry in the study of the total cavopulmonary connection: Computational simulations and *in vitro* experiments. *Ann. Biomed. Eng.* 29:844–853, 2001.

[54]Saber, N. R., A. D. Gosman, N. B. Wood, P. J. Kilner, C. L. Charrier, and D. N. Firmin. Computational flow modeling of the left ventricle based on *in vivo* MRI data: Initial experience. *Ann. Biomed. Eng.* 29:275–283, 2001.

[55]Shahcheraghi, N., H. A. Dwyer, A. Y. Cheer, A. I. Barakat, and T. Rutaganira. Unsteady and three-dimensional simulation of blood flow in the human aortic arch. *J. Biomech. Eng.* 124:378–397, 2002.

[56]Sharma, S., A. E. Ensley, K. Hopkins, G. P. Chatzimavroudis, T. M. Healy, V. H. K. Tam, K. R. Kanter, and A. P. Yoganathan. *In vivo* flow dynamics of the total cavopulmonary connection from three-dimensional multi slice magnetic resonance imaging. *Ann. Thorac. Surg.* 71:889–898, 2001.

[57]Sheu, T. W. H., S. F. Tsai, W. S. Hwang, and T. M. Chang. A finite element study of the blood flow in total cavopulmonary connection. *Comput. Fluids* 28:19–39, 1999.

[58]Special issue on verification and validation in CFD. *AIAA J.* 36(5), 1998.

[59]Swann, S. Integration of MRI and stereolithography to build medical models: A case study. *Rapid Prototyp. J.* 2(4):41–46, 1996.

[60]Tang, H. S., S. C. Jones, and F. Sotiropoulos. An overset-grid method for 3D unsteady incompressible flows. *J. Comput. Phys.* 191(2):567–600, 2003.

[61]Thomas, J. B., J. S. Milner, B. K. Rutt, and D. A. Steinman. Reproducibility of image-based computational fluid dynamics models of the human carotid bifurcation. *Ann. Biomed. Eng.* 31:132–41, 2003.

[62]NATO Advisory Group for Aeronautical Research and Development. Validation of Computational Fluid Dynamics. Portugal: NATO Advisory Group for Aeronautical Research and Development, AGARD CP 437, December 1988.

[63]Van Haesdonck, J. M., L. Mertens, R. Sizaire, G. Montas, B. Purnode, W. Daenen, M. Crochet, and M. Gewling. Comparisons by computerized numeric modeling of energy losses in different Fontan connections. *Circulation* 92:322–326, 1995.

[64]Verdonck, P. Guest Editorial, The role of computational fluid dynamics for artificial organ design. *Artif. Organs* 26(7):569–570, 2002.

[65]Workshop, British Heart Foundation, Imperial College, London: Breaking Symmetry in Haemodynamics. *Biorheology* (Special Issue), 39(3–4):289–575, 2001.

[66]Yedavalli, R. V., F. Loth, A. Yardimci, W. F. Pritchard, J. N. Oshinski, L. Sadler, F. Charbel, and N. Alperin. Construction of a physical model of the human carotid artery based upon *in vivo* magnetic resonance images. *J. Biomech. Eng.* 123:372–376, 2001.

[67]Zhang, X., D., Schimdt, and B. Perot. Accuracy and conservation properties of a three-dimensional unstructured staggered mesh scheme for fluid dynamics. *J. Comput. Phys.* 175(2):764–791, 2002.